

Characterization of Aerosol and CO₂ Co-Emissions around Power Plants through Satellite-Based Synergistic Observations

Lu Sun ^{1,2} , Siqi Yu ^{1,3,*} and Dong Liu ⁴ ¹ Jianghuai Advance Technology Center, Hefei 230000, China; lsun819@aucklanduni.ac.nz² Department of Physics, The University of Auckland, Auckland 1010, New Zealand³ Department of Earth System Science, Tsinghua University, Beijing 100084, China⁴ Key Laboratory of Atmospheric Optics, Anhui Institute of Optics and Fine Mechanics, Chinese Academy of Sciences, Hefei 230031, China; dliu@aiofm.cas.cn

* Correspondence: yusq@mail.ustc.edu.cn

Abstract: The tracking of carbon and aerosol co-emissions is essential for environmental management. Satellite-based atmospheric synoptic observation networks provide large-scale and multifaceted data to help resolve emission behaviors. This study employs a comprehensive analysis of atmospheric dynamics, combustion byproducts, and aerosol characteristics around power plants. Strong correlations between Aerosol Optical Depth (AOD) at 500 nm and the column-averaged dry-air mole fraction of carbon dioxide (XCO₂) were observed, revealing synchronous peaks in their emission patterns. The investigation into combustion completeness utilized metrics such as the ratio of carbon monoxide (CO)/XCO₂ and Black Carbon Extinction (BCEXT)/Total Aerosol Extinction (TOTEXT). Discrepancies in these ratios across cases suggest variations in combustion efficiency and aerosol characteristics. Nitrogen dioxide (NO₂) distributions closely mirrored XCO₂, indicating consistent emission patterns, while variations in sulfur dioxide (SO₂) distributions implied differences in sulfide content in the coal used. The influence of coal composition on AOD/XCO₂ ratios was evident, with sulfide content contributing to variations besides combustion efficiency. This multifactorial analysis underscores the complex interplay of combustion completeness, aerosol composition, and coal components in shaping the air quality around power stations. The findings highlight the need for a nuanced understanding of these factors for effective air quality management.

Keywords: pollution emission; CO₂ emission; satellite monitoring; pollution mitigation; emission reduction



Citation: Sun, L.; Yu, S.; Liu, D. Characterization of Aerosol and CO₂ Co-Emissions around Power Plants through Satellite-Based Synergistic Observations. *Remote Sens.* **2024**, *16*, 1609. <https://doi.org/10.3390/rs16091609>

Academic Editor: Alexander Kokhanovsky

Received: 20 March 2024

Revised: 25 April 2024

Accepted: 29 April 2024

Published: 30 April 2024



Copyright: © 2024 by the authors. Licensee MDPI, Basel, Switzerland. This article is an open access article distributed under the terms and conditions of the Creative Commons Attribution (CC BY) license (<https://creativecommons.org/licenses/by/4.0/>).

1. Introduction

The urgent global imperative to address climate change has spurred innovative approaches aimed at comprehensively understanding and mitigating the impact of carbon dioxide (CO₂) emissions on our environment [1–8]. Carbon peak and carbon neutrality have risen to prominence worldwide as guiding principles for climate action [9–13]. Simultaneously, carbon dioxide observations have emerged as a critical enabler in achieving these ambitious goals [14–18].

One of the primary sources of anthropogenic carbon dioxide is burning fossil fuels. This process is also among the most important sources of anthropogenic aerosols [19–22]. The combined monitoring of carbon dioxide and aerosols plays a crucial role in verifying the features of complex emissions [23–25]. Numerous long-term projects have been initiated to investigate aerosol properties, yielding substantial observational findings across various scales. However, observations of carbon dioxide exhibit discontinuities in both spatial and temporal dimensions. The aerosol observational results could significantly enhance our understanding of carbon dioxide observations if a more precise correlation between carbon dioxide and aerosols is revealed [26–28]. Previous research has identified significant correlations between carbon monoxide and aerosol [29–31]. It indicates that carbon dioxide and aerosols should have similar correlations. The existing research investigating

the relationship between carbon dioxide and aerosols primarily relies on ground-based data [32]. To ensure representative assessment with wide observation coverage, multi-satellite datasets need to be employed to make it possible to track the emission of aerosols and carbon dioxide around the coal-fired power plants, which are the main contributors to complex emissions and air pollution [33,34].

The purpose of this study was to compare the emissions of CO₂ and aerosols around several coal-fired power plants to reveal their potential correlation. The correlations can be employed to establish a relationship between the column-averaged dry-air mole fraction of carbon dioxide (XCO₂) and Aerosol Optical Depth (AOD), which has been extensively observed and documented. Based on Orbiting Carbon Observatory-2 (OCO-2) and Himawari-8 satellite observations, the emission enhancements of the XCO₂ and AOD around the power plants were obtained and found to be in good agreement. Utilizing pollutant gas emissions monitored by Tropospheric Monitoring Instrument (TROPOMI) and combining them with carbon data from Modern-Era Retrospective Analysis for Research and Applications, version 2 (MERRA-2), we synthetically analyzed the emission discrepancies and their potential significance. Understanding the correlation between CO₂ and aerosol emissions from the same power plant will have significant benefits in helping us resolve the emission characteristics and promote the goals of carbon neutrality and air quality improvement [35].

2. Data and Methods

2.1. Satellite Observations

OCO-2 is a satellite mission with the goal of studying the earth's carbon cycle to help atmospheric scientists better understand the sources and sinks of CO₂ [36]. OCO-2 is part of the National Aeronautics and Space Administration (NASA)'s Earth System Science Pathfinder (ESSP) program and was launched on 2 July 2014 [37,38]. The satellite carries a high-resolution spectrometer to measure the concentration of CO₂ in the earth's atmosphere [39]. By monitoring the distribution of CO₂ in the atmosphere, OCO-2 contributes to our understanding of how greenhouse gases contribute to climate change and helps us track and mitigate the impact of human activities on the global carbon cycle [40,41].

Himawari-8, the geostationary weather satellite operated by the Japan Meteorological Agency (JMA), was launched into space in 2014. It is part of the Himawari series of satellites and plays a crucial role in monitoring weather, atmospheric conditions, and climate in the Asia-Pacific region. These satellites provide high-resolution, real-time imagery of the earth's surface and atmosphere from a geostationary orbit, which means they stay fixed in the same position relative to the earth, allowing continuous monitoring of a specific region. Himawari-8 is equipped with advanced sensors, including a multi-spectral imager and a sounder, which provide data for weather forecasting and climate monitoring [42,43]. Himawari-8 has an AOD product (at 0.5 μm) derived from full-disk observations conducted during the daytime. AOD is retrieved from the lookup table, which represents the theoretical relationships between Advanced Himawari Imager (AHI) visible and near-infrared reflectance and aerosol properties compiled from radiative transfer simulation.

The TROPOMI was co-funded by the European Space Agency (ESA) and the Netherlands and is a space-borne, nadir-viewing imaging spectrometer that covers wavelength bands between ultraviolet and shortwave infrared [44,45]. It measures a range of trace gases, including nitrogen dioxide (NO₂), sulfur dioxide (SO₂), and carbon monoxide (CO), at fine spatial resolution with daily global coverage and is onboard the Sentinel-5 Precursor satellite [46]. Because of their high resolution, this new generation of satellite instruments, like TROPOMI, provides enough detail to contribute to air pollution and emission monitoring at the regional and local scales [47]. In this study, the TROPOMI observational results are utilized to analyze the combustion of coal together with the CO₂ emission observed by OCO-2.

2.2. MERRA-2 Reanalysis Product

MERRA-2 (Modern-Era Retrospective Analysis for Research and Applications, version 2) is a reanalysis dataset created by NASA that provides a comprehensive and consistent record of the earth's climate from the surface to the top of the atmosphere [48,49]. It includes various atmospheric variables, including aerosol concentrations, and is widely used by researchers and scientists for climate and environmental studies. MERRA-2 provides information on aerosol concentrations at different altitudes and in various regions of the world. The Goddard Aerosol Assimilation System (GAAS) is used in MERRA-2. GAAS includes 15 aerosol tracers (dust, sea salt, sulfate, and black and organic carbon) whose lifetime is driven by prescribed sea-surface temperature and sea ice, daily volcanic and biomass burning emissions, as well as high-resolution inventories of anthropogenic emission sources [50,51].

2.3. Power Plant and Data Matching

According to the matching pattern between multiple sources of data, we identified four examples to organize the analysis, corresponding to four coal-fired power plants. The geolocation information of four coal-fired power plants in China is obtained from the Global Power Plant Database (GPPD) [52], as listed in Table 1. The power plant selection criteria are as follows: (1) Coal is the primary fuel. (2) The power plants are located less than 10 km from the nearest OCO-2 orbits. Since the primary fuel of these four power plants is coal, there will be many daily aerosols due to the complete combustion (organic carbon aerosol) or incomplete combustion (black carbon aerosol) and carbon emissions from these sites. They are ideal targets for studying the correlation between XCO₂ and aerosol emissions from individual power plants.

Table 1. The locations of the power plant cases in this study.

Number	Name	Location	Primary Fuel
Case 1 (20 July 2020)	Zouping Huineng Thermal Power Co., Ltd.	117.86°E, 36.90°N	Coal
Case 2 (22 May 2019)	Datang Wuan Power Generation Co., Ltd.	114.19°E, 36.82°N	Coal
Case 3 (21 January 2019)	Huaneng Baotou No. 1 power station Co., Ltd.	109.66°E, 40.66°N	Coal
Case 4 (16 October 2021)	Shanxi Shentou power station Co., Ltd.	112.49°E, 39.55°N	Coal

By analyzing the OCO-2 and Himawari-8 products, the orbit of OCO-2 can pass the power plants occasionally. It is expected to simultaneously obtain the AOD retrievals from Himawari-8 and the retrieved XCO₂ located near the power plants. Thus, when the track of OCO-2 was close to the power plant, we matched the time of the Himawari-8 with the time of OCO-2 passing the power plant, and then matched the grid data of the Himawari-8 with the latitude and longitude data of OCO-2. OCO-2 only has one orbit at a specific time and location. Therefore, it cannot observe the same location continuously. Unlike the OCO-2, Himawari-8 observations are continuous at specific points because it is a geostationary satellite. Similarly, we matched the TROPOMI data for OCO-2. For the surface wind and MERRA-2 data, we used the time at which OCO-2 passes the power plant as a matching criterion, and it is worth noting that for the MERRA-2 data, no OCO-2 latitude/longitude matching was performed. Instead, the data around the power plant were utilized for the analysis. The data products mentioned above are shown in Table 2. In order to capture the incremental portion of the data generated by the power plant, it is necessary to identify the background baseline and then obtain the increments based on striking changes along the baseline. We present a schematic representation of the background and increment in Figure 1c. The distinct enhancement variation on the baseline allows us to identify the location of the striking change and to identify the background and increment parts.

The increment of MERRA data, including Black Carbon Extinction (BCEXT@550nm) and Total Aerosol Extinction (TOTEXT@550 nm), is derived from the nine-point grid data surrounding the power plant by subtracting the nine-point grid average from the center grid data of the area in which the power plant is located.

Table 2. Observation and model products used for this study.

Satellite/Model	Product	Temporal Resolution	Spatial Resolution (lon × lat)	Quality Control
OCO-2	XCO ₂	/	1.29° × 2.25°	quality_flag = 1
Himawari-8	AOD@500nm	10 min	0.05° × 0.05°	confidence ≥ good
TROPOMI	NO ₂ , SO ₂	/	3.5 × 5.5 km ² (3.5 × 7 km ² before August 2019)	qa_value > 0.5
TROPOMI	CO	/	7 × 5.5 km ² (7 × 7 km ² before August 2019)	qa_value > 0.5
MERRA-2	BCEXT@550nm, TOTEXT@550nm	60 min	0.625° × 0.5°	/
ERA5	Wind@1000hPa	60 min	0.25° × 0.25°	/

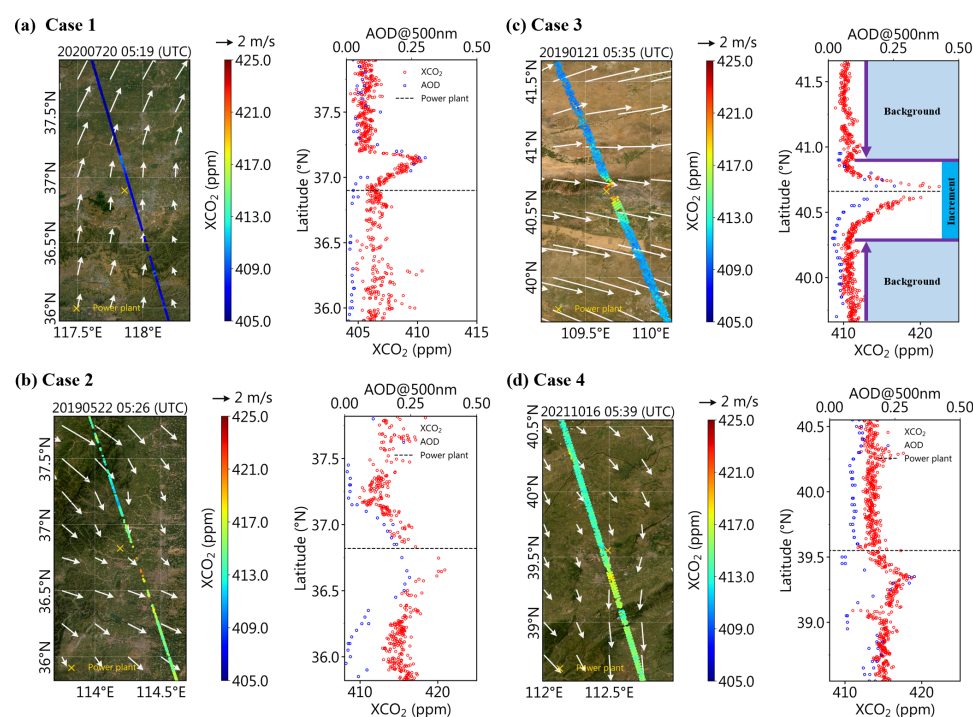


Figure 1. XCO₂ (the column-averaged dry-air mole fraction of carbon dioxide) and AOD (aerosol optical depth) at 500 nm over four different power stations: (a) Case 1: Zouping Huineng Thermo Power Co., Ltd. (b) Case 2: Datang Wuan Power Generation Co., Ltd. (c) Case 3: Huaneng Baotou No. 1 power station Co., Ltd. (d) Case 4: Shanxi Shentou power station Co., Ltd. Wind speed and direction are overplotted to indicate the meteorological conditions around the power stations. Each exact location of the power station is marked in yellow and centered on the color maps. The dotted line represents the latitude position of the power plant. A schematic of the background and increment is illustrated in Case 3.

3. Results and Discussion

Figure 1 illustrates the XCO₂ and AOD at 500 nm across four distinct power stations, as outlined in Table 1. The selected orbits of the OCO-2 closely align with the locations of these power stations, enabling the accurate depiction of CO₂ emitted from these facilities. Notably, AODs at 500 nm exhibit strong correlations with XCO₂ in all four instances. The correlation coefficient is 0.73, 0.78, 0.63, and 0.71, respectively, from Figure 1a–d.

The influence of surrounding wind fields becomes apparent in the displacement of areas with the highest XCO₂ from the power stations. As depicted in Figure 1a, along the

orbit, the pixels exhibiting the highest XCO₂ are situated north of the power station due to the prevailing south wind direction, guiding emitted CO₂ in that direction. Intriguingly, the scatter plot reveals a synchronous peak between AOD and XCO₂. In cases 2 and 3, the locations with the highest XCO₂ are in closer proximity to the power stations. Case 2 experiences lower wind speeds and a more erratic wind direction compared to Case 1, potentially impeding the transportation of CO₂ and aerosols. In Case 3, despite high wind speeds, the power station's location in a valley constrains the dispersion of CO₂ and aerosols.

The observed correlation between XCO₂ and AOD is likely attributed to the varied nature of coal combustion, encompassing both complete and incomplete processes. Distinct combustion characteristics and coal components can contribute to divergent connections between AOD and XCO₂. In Figure 2, the backdrop of AOD and XCO₂ has been subtracted to scrutinize the association between the incremental changes in AOD and XCO₂. This deduction aims to isolate the specific relationship between the increase in AOD and the corresponding rise in XCO₂, providing a clearer understanding of their interdependence.

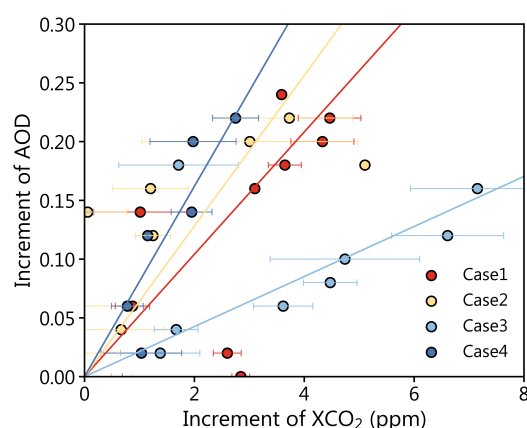


Figure 2. Increments of AOD (aerosol optical depth) and XCO₂ (the column-averaged dry-air mole fraction of carbon dioxide) for the four cases, as introduced in Figure 1. Colored lines indicate linear fitting results.

In Figure 2, the correlation between the increase in AOD and the corresponding rise in XCO₂ is illustrated for the four power station cases. The increment is determined by calculating the peak value around each power station and subtracting the background. The background is determined by referencing values at the tails of the XCO₂, as depicted in Figure 1. Notably, for AOD, the observations are aligned with the OCO-2 orbits before the background is computed. This approach ensures a precise calculation of the background against which the AOD increments are assessed.

The ratio between the increment of AOD and the increment of XCO₂ varies across different cases, suggesting distinct post-combustion components. Drawing inspiration from the study findings presented in [46], in which emission factors (EFs) of nitrogen oxides (NO_x) and CO served as indicators of combustion efficiency, our research aligns with this approach. As depicted in Figure 2, case 3 exhibits the lowest AOD/XCO₂ ratio, while case 4 has the highest. Notably, case 2's ratio surpasses that of case 1. A higher ratio indicates a greater increase in AOD relative to XCO₂, implying more complete combustion. Conversely, a lower ratio indicates reduced AOD alongside elevated CO₂ emissions, suggesting either a lack of aerosols from combustion or aerosol components with lower extinction coefficients.

The increase in AOD can be attributed to two primary factors: a rise in aerosol concentration and alterations in the morphology and components of aerosols, represented by the extinction coefficient of aerosols. Both scenarios can occur when combustion is incomplete. However, tracking specific aerosol components or the distribution of extinction coefficients in the column proves challenging. To investigate the completeness of combustion, the relationship between the increment of CO and the increment of XCO₂ in Figure 3 is explored.

The assumption here is that if combustion is complete, there will be minimal CO emitted into the atmosphere. Consequently, the ratio of CO/XCO₂ will be lower, and vice versa, providing insights into the degree of combustion completeness.

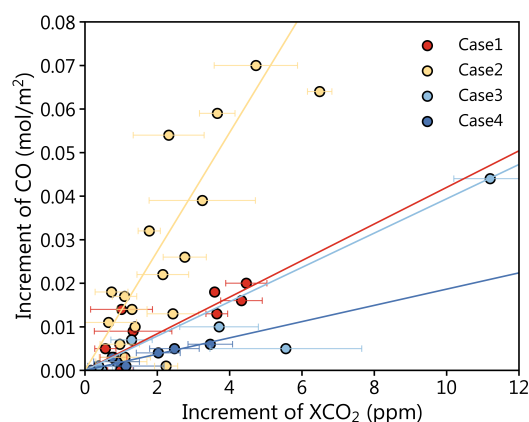


Figure 3. Increments of CO (carbon monoxide) and XCO₂ (the column-averaged dry-air mole fraction of carbon dioxide) for the four cases. Colored lines indicate linear fitting results.

In Figure 3, case 4 has the lowest CO/XCO₂ ratio and case 2 has the highest. We expect to see that the CO/XCO₂ ratios of the cases are proportional to the AOD/XCO₂ ratios. However, the results are not aligned with the expectations. For example, case 4 has the largest AOD/XCO₂ ratio but has the least CO/XCO₂ ratio. This indicates that the completeness of combustion may not be the main reason for the different AOD/XCO₂ ratios.

In Figure 4, the ratio between BCEXT and TOTEXT is presented, as calculated from the MERRA-2 dataset. Interestingly, the cases with high (low) CO/XCO₂ ratios do not align consistently with those that have high (low) BCEXT/TOTEXT ratios. Case 2 stands out with the highest BCEXT/TOTEXT ratio, and also with the highest CO/XCO₂ ratio. Case 1 surpasses case 3 in BCEXT/TOTEXT and in CO/XCO₂. The exception is case 4, which, based on the CO/XCO₂ ratio metric, indicates the most complete combustion. However, according to the BCEXT/TOTEXT ratio metric, case 4's result is higher than that of cases 1 and 3.

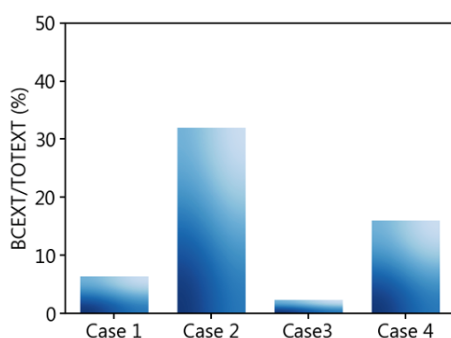


Figure 4. The ratio of BCEXT (black carbon extinction) to TOTEXT (total extinction) for the four cases.

In Figure 5, the distributions of two additional components, namely NO₂ and SO₂, are presented alongside CO and CO₂. This comprehensive view acknowledges that the components emitted as a result of combustion extend beyond CO₂ and CO. Analyzing the presence of these additional components helps elucidate the potential composition of coal used in the four power stations and provides insights into the reasons behind variations in AOD changes and combustion completeness. The distributions of NO₂ closely mirror those of XCO₂, suggesting a consistent emission pattern. However, the distributions of SO₂ exhibit considerable variation. While the peaks of SO₂ roughly coincide with XCO₂, except for case 4, the remaining portions of the distributions display some discrepancies.

This variation implies differences in the sulfide content of the coal used in the power stations. Given the significance of SO_2 in the formation of secondary organic aerosol (SOA), this diversity in coal composition contributes to the observed differences in AOD/ XCO_2 ratios, underscoring the multifaceted factors influencing combustion outcomes.

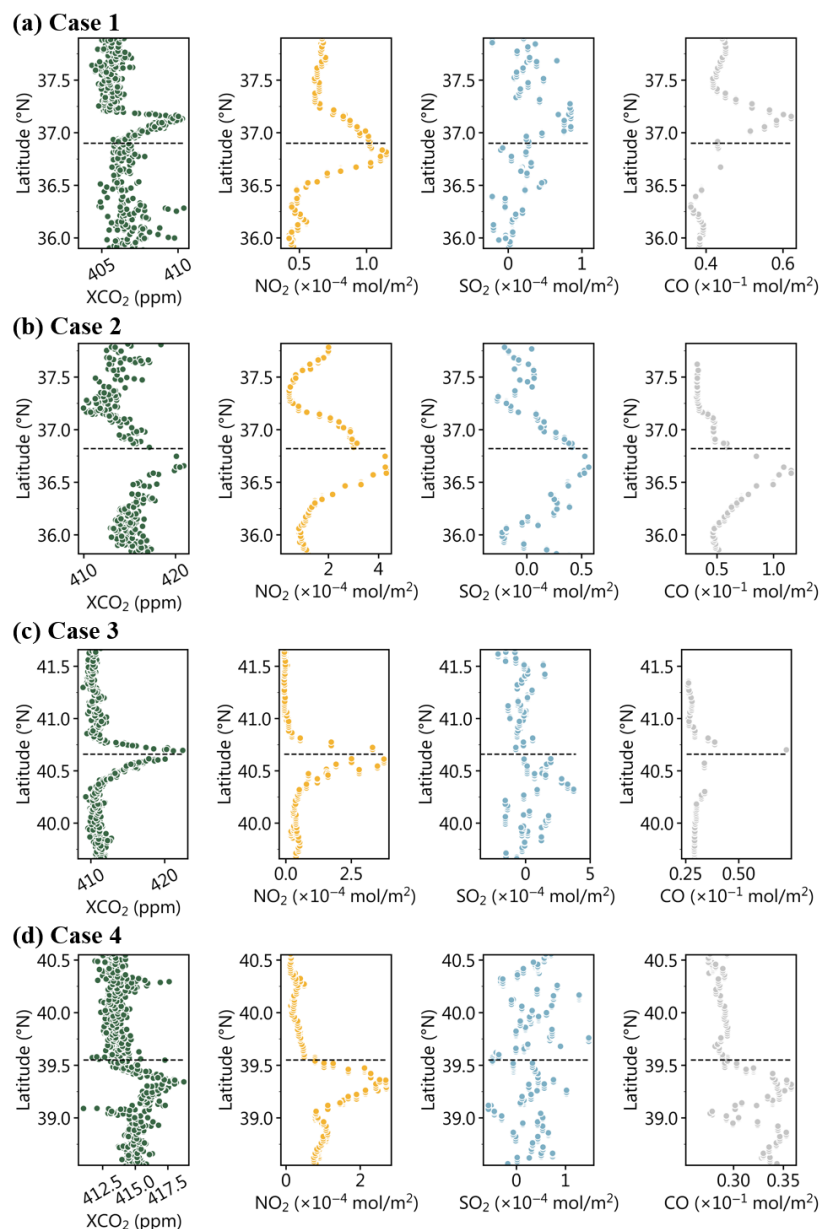


Figure 5. Comparisons of the typical chemical compositions, XCO_2 (the column-averaged dry-air mole fraction of carbon dioxide), NO_2 (nitrogen dioxide), SO_2 (sulfur dioxide), and CO (carbon monoxide) emitted by the four power plants. The dotted line represents the latitude position of the power plant.

In Table 3, we calculated the Pearson correlation coefficients of the three gases with XCO_2 according to Figure 5. Our findings were consistent with Figure 5, indicating that XCO_2 and CO have the highest correlation coefficient, while XCO_2 and SO_2 exhibit the most variation. One of the possible reasons for this is the existence of wavelength sensitivity for ozone (O_3). The SO_2 absorption signature suffers from interference with the ozone absorption spectrum [53]. The coal-fired power stations emit large amounts of nitrogen oxides, contributing to rising ozone levels. Thus, the challenge of accurately monitoring the SO_2 around the coal-fired power stations has arisen.

Table 3. Correlation coefficients between XCO₂ (the column-averaged dry-air mole fraction of carbon dioxide) and the three gases of NO₂ (nitrogen dioxide), SO₂ (sulfur dioxide) and CO (carbon monoxide) profiled in Figure 5.

Case Number	XCO ₂ – NO ₂	XCO ₂ – SO ₂	XCO ₂ – CO
Case 1	0.36 *	0.48 *	0.70 *
Case 2	0.71 *	0.82 *	0.84 *
Case 3	0.89 *	0.20 *	0.79 *
Case 4	0.84 *	0.18 *	0.83 *

* $p < 0.05$.

4. Conclusions

In this paper, we analyze the XCO₂ derived from OCO-2 and AOD retrieved from Himawari-8 around four coal-based power plants to explore the correlation between XCO₂ and AOD. The results have unveiled a complex interplay of factors that influence air quality. The robust correlation observed between AOD and XCO₂ underlines the significance of aerosol optical properties in understanding CO₂ emissions.

Metrics such as the CO/XCO₂ and BCEXT/TOTEXT ratios provided valuable insights into combustion completeness. However, discrepancies in these ratios across cases indicated that factors beyond combustion efficiency play a role, prompting a closer examination of aerosol composition. The consistent distribution of NO₂ with XCO₂ suggested uniform emission patterns, while variations in SO₂ distributions indicated potential differences in sulfide content within coal sources.

The intricate relationship between coal composition and AOD/XCO₂ ratios further emphasized the need for a nuanced understanding of aerosol characteristics. Sulfide content, which has implications for secondary organic aerosol formation, emerged as a significant contributor to the observed variations. This multifactorial analysis underscores the complex nature of air quality dynamics around power stations, necessitating a comprehensive approach to effective management and mitigation strategies.

Aerosol optical depth observations have been globally deployed for approximately two decades, encompassing both in situ and satellite data. The precision and coverage of aerosol observations significantly surpass those of CO₂. This study underscores the potential to derive XCO₂ from the obtained aerosol data:

$$\text{AOD/XCO}_2 = f(\text{degree of combustion, components of combustion emission})$$

$$\text{XCO}_2 = \text{AOD}/f(\text{degree of combustion, components of combustion emission}).$$

where f represents a function intricately linked to both the degree of combustion and the components constituting aerosols. The degree of combustion is quantifiable through metrics such as CO/XCO₂, providing a measurable indicator of combustion efficiency. Simultaneously, discerning the components within combustion emissions involves a comprehensive analysis of the coal composition utilized in power stations. The intricate interplay of these variables within function f enables a holistic understanding of the aerosol dynamics and combustion characteristics under consideration.

The limitations of this study are as follows: (1) The number of power stations is limited, so it is unable to reveal more details about how the degree of combustion and the components of combustion emission affect the AOD/XCO₂ ratios. (2) There is a lack of black carbon extinction observations close to the chosen power plants. MERRA-2 data are available, however, there are still large uncertainties associated with MERRA-2 data in aerosol simulation [54–57].

In future studies, more power stations will be analyzed. Our research will contribute to the growing body of knowledge on the intricate interactions that shape air quality, providing valuable insights for policymakers and researchers engaged in the pursuit of sustainable and efficient energy practices. More in situ observations will be incorporated for comparison with the remote sensing results. The final functions linking the degree of combustion and the components constituting aerosols are expected to be built for each coal-fired power plant.

Author Contributions: Conceptualization, S.Y.; methodology, L.S.; software, L.S.; validation, L.S. and S.Y.; resources, L.S.; data curation, L.S.; writing—original draft preparation, L.S.; writing—review and editing, L.S. and S.Y.; visualization, L.S.; supervision, D.L.; project administration, D.L.; funding acquisition, S.Y. All authors have read and agreed to the published version of the manuscript.

Funding: The work was supported by the Dreams Foundation of Jianghuai Advance Technology Center (No. 2023-ZM01K008).

Data Availability Statement: Power plant information can be found in <https://datasets.wri.org/dataset/globalpowerplantdatabase> (accessed on 1 February 2024). OCO-2 data can be downloaded from <https://ocov2.jpl.nasa.gov/science/oco-2-data-center/> (accessed on 1 February 2024). Himawari data can be downloaded from https://www.data.jma.go.jp/mscweb/en/himawari89/cloud_service/cloud_service.html (accessed on 1 February 2024). MERRA-2 product is from <https://disc.gsfc.nasa.gov/datasets?project=MERRA-2> (accessed on 1 February 2024). ERA5 data is from <https://www.ecmwf.int/en/forecasts/dataset/ecmwf-reanalysis-v5> (accessed on 1 February 2024).

Conflicts of Interest: The authors declare no conflicts of interest.

References

1. Socolow, R.; Hotinski, R.; Greenblatt, J.; Pacala, S. Solving the climate problem: Technologies available to curb CO₂ emissions. *Environment* **2004**, *46*, 8–19. [\[CrossRef\]](#)
2. Solomon, S.; Plattner, G.K.; Knutti, R.; Friedlingstein, P. Irreversible climate change due to carbon dioxide emissions. *Proc. Natl. Acad. Sci. USA* **2009**, *106*, 1704–1709. [\[CrossRef\]](#) [\[PubMed\]](#)
3. Nema, P.; Nema, S.; Roy, P. An overview of global climate changing in current scenario and mitigation action. *Renew. Sustain. Energy Rev.* **2012**, *16*, 2329–2336. [\[CrossRef\]](#)
4. Friedlingstein, P.; Andrew, R.M.; Rogelj, J.; Peters, G.P.; Canadell, J.G.; Knutti, R.; Luderer, G.; Raupach, M.R.; Schaeffer, M.; van Vuuren, D.P.; et al. Persistent growth of CO₂ emissions and implications for reaching climate targets. *Nat. Geosci.* **2014**, *7*, 709–715. [\[CrossRef\]](#)
5. Keller, D.P.; Feng, E.Y.; Oschlies, A. Potential climate engineering effectiveness and side effects during a high carbon dioxide-emission scenario. *Nat. Commun.* **2014**, *5*, 3304. [\[CrossRef\]](#) [\[PubMed\]](#)
6. Rogelj, J.; Schaeffer, M.; Meinshausen, M.; Shindell, D.T.; Hare, W.; Klimont, Z.; Velders, G.J.M.; Amann, M.; Schellnhuber, H.J. Disentangling the effects of CO₂ and short-lived climate forcer mitigation. *Proc. Natl. Acad. Sci. USA* **2014**, *111*, 16325–16330. [\[CrossRef\]](#) [\[PubMed\]](#)
7. Mac Dowell, N.; Fennell, P.S.; Shah, N.; Maitland, G.C. The role of CO₂ capture and utilization in mitigating climate change. *Nat. Clim. Chang.* **2017**, *7*, 243–249. [\[CrossRef\]](#)
8. Ma, R.; Abid, N.; Yang, S.; Ahmad, F. From crisis to resilience: Strengthening climate action in OECD countries through environmental policy and energy transition. *Environ. Sci. Pollut. Res. Int.* **2023**, *30*, 115480–115495. [\[CrossRef\]](#) [\[PubMed\]](#)
9. Chen, J.; Cui, H.; Xu, Y.; Ge, Q. Long-term temperature and sea-level rise stabilization before and beyond 2100: Estimating the additional climate mitigation contribution from China’s recent 2060 carbon neutrality pledge. *Environ. Res. Lett.* **2021**, *16*, 074032. [\[CrossRef\]](#)
10. Liu, Z.; Deng, Z.; He, G.; Wang, H.; Zhang, X.; Lin, J.; Qi, Y.; Liang, X. Challenges and opportunities for carbon neutrality in China. *Nat. Rev. Earth Environ.* **2022**, *3*, 141–155. [\[CrossRef\]](#)
11. Wu, Z.; Huang, X.; Chen, R.; Mao, X.; Qi, X. The United States and China on the paths and policies to carbon neutrality. *J. Environ. Manag.* **2022**, *320*, 115785. [\[CrossRef\]](#) [\[PubMed\]](#)
12. Xu, G.; Dong, H.; Xu, Z.; Bhattarai, N. China can reach carbon neutrality before 2050 by improving economic development quality. *Energy* **2022**, *243*, 123087. [\[CrossRef\]](#)
13. Zhang, S.; Chen, W. Assessing the energy transition in China towards carbon neutrality with a probabilistic framework. *Nat. Commun.* **2022**, *13*, 87. [\[CrossRef\]](#) [\[PubMed\]](#)
14. Kort, E.A.; Frankenberg, C.; Miller, C.E.; Oda, T. Space-based observations of megacity carbon dioxide. *Geophys. Res. Lett.* **2012**, *39*, L17806. [\[CrossRef\]](#)
15. Mitchell, L.E.; Lin, J.C.; Bowling, D.R.; Pataki, D.E.; Strong, C.; Schauer, A.J.; Bares, R.; Bush, S.E.; Stephens, B.B.; Mendoza, D.; et al. Long-term urban carbon dioxide observations reveal spatial and temporal dynamics related to urban characteristics and growth. *Proc. Natl. Acad. Sci. USA* **2018**, *115*, 2912–2917. [\[CrossRef\]](#) [\[PubMed\]](#)
16. Liu, F.; Duncan, B.N.; Krotkov, N.A.; Lamsal, L.N.; Beirle, S.; Griffin, D.; McLinden, C.A.; Goldberg, D.L.; Lu, Z. A methodology to constrain carbon dioxide emissions from coal-fired power plants using satellite observations of co-emitted nitrogen dioxide. *Atmos. Chem. Phys.* **2020**, *20*, 99–116. [\[CrossRef\]](#)
17. Zheng, B.; Chevallier, F.; Ciais, P.; Broquet, G.; Wang, Y.; Lian, J.; Zhao, Y. Observing carbon dioxide emissions over China’s cities and industrial areas with the Orbiting Carbon Observatory-2. *Atmos. Chem. Phys.* **2020**, *20*, 8501–8510. [\[CrossRef\]](#)

18. MacDonald, C.G.; Mastrogiacomo, J.P.; Laughner, J.L.; Hedelius, J.K.; Nassar, R.; Wunch, D. Estimating enhancement ratios of nitrogen dioxide, carbon monoxide and carbon dioxide using satellite observations. *Atmos. Chem. Phys.* **2023**, *23*, 3493–3516. [[CrossRef](#)]
19. Wolf, M.; Hidy, G. Aerosols and climate: Anthropogenic emissions and trends for 50 years. *J. Geophys. Res.-Atmos.* **1997**, *102*, 11113–11121. [[CrossRef](#)]
20. Turnbull, J.C.; Karion, A.; Fischer, M.L.; Faloona, I.; Guilderson, T.; Lehman, S.J.; Miller, B.R.; Miller, J.B.; Montzka, S.; Sherwood, T.; et al. Assessment of fossil fuel carbon dioxide and other anthropogenic trace gas emissions from airborne measurements over Sacramento, California in spring 2009. *Atmos. Chem. Phys.* **2011**, *11*, 705–721. [[CrossRef](#)]
21. Lelieveld, J.; Klingmueller, K.; Pozzer, A.; Burnett, R.T.; Haines, A.; Ramanathan, V. Effects of fossil fuel and total anthropogenic emission removal on public health and climate. *Proc. Natl. Acad. Sci. USA* **2019**, *116*, 7192–7197. [[CrossRef](#)] [[PubMed](#)]
22. Lei, R.; Feng, S.; Lauvaux, T. Country-scale trends in air pollution and fossil fuel CO₂ emissions during 2001–2018: Confronting the roles of national policies and economic growth. *Environ. Res. Lett.* **2021**, *16*, 014006. [[CrossRef](#)]
23. Guerlet, S.; Butz, A.; Schepers, D.; Basu, S.; Hasekamp, O.P.; Kuze, A.; Yokota, T.; Blavier, J.F.; Deutscher, N.M.; Griffith, D.W.T.; et al. Impact of aerosol and thin cirrus on retrieving and validating XCO₂ from GOSAT shortwave infrared measurements. *J. Geophys. Res.-Atmos.* **2013**, *118*, 4887–4905. [[CrossRef](#)]
24. Schneising, O.; Heymann, J.; Buchwitz, M.; Reuter, M.; Bovensmann, H.; Burrows, J.P. Anthropogenic carbon dioxide source areas observed from space: Assessment of regional enhancements and trends. *Atmos. Chem. Phys.* **2013**, *13*, 2445–2454. [[CrossRef](#)]
25. Sanghavi, S.; Nelson, R.; Frankenberg, C.; Gunson, M. Aerosols in OCO-2/GOSAT retrievals of XCO₂: An information content and error analysis. *Remote Sens. Environ.* **2020**, *251*, 112053. [[CrossRef](#)]
26. Houweling, S.; Hartmann, W.; Aben, I.; Schrijver, H.; Skidmore, J.; Roelofs, G.; Breon, F. Evidence of systematic errors in SCIAMACHY-observed CO₂ due to aerosols. *Atmos. Chem. Phys.* **2005**, *5*, 3003–3013. [[CrossRef](#)]
27. Eldering, A.; O'Dell, C.W.; Wennberg, P.O.; Crisp, D.; Gunson, M.R.; Viatte, C.; Avis, C.; Braverman, A.; Castano, R.; Chang, A.; et al. The Orbiting Carbon Observatory-2: First 18 months of science data products. *Atmos. Meas. Tech.* **2017**, *10*, 549–563. [[CrossRef](#)]
28. Liu, Y.; Wang, J.; Yao, L.; Chen, X.; Cai, Z.; Yang, D.; Yin, Z.; Gu, S.; Tian, L.; Lu, N.; et al. The TanSat mission: Preliminary global observations. *Sci. Bull.* **2018**, *63*, 1200–1207. [[CrossRef](#)]
29. Spackman, J.R.; Schwarz, J.P.; Gao, R.S.; Watts, L.A.; Thomson, D.S.; Fahey, D.W.; Holloway, J.S.; de Gouw, J.A.; Trainer, M.; Ryerson, T.B. Empirical correlations between black carbon aerosol and carbon monoxide in the lower and middle troposphere. *Geophys. Res. Lett.* **2008**, *35*, L19816. [[CrossRef](#)]
30. Burling, I.R.; Yokelson, R.J.; Akagi, S.K.; Urbanski, S.P.; Wold, C.E.; Griffith, D.W.T.; Johnson, T.J.; Reardon, J.; Weise, D.R. Airborne and ground-based measurements of the trace gases and particles emitted by prescribed fires in the United States. *Atmos. Chem. Phys.* **2011**, *11*, 12197–12216. [[CrossRef](#)]
31. Lalitaporn, P.; Mekaumnayachai, T. Satellite measurements of aerosol optical depth and carbon monoxide and comparison with ground data. *Environ. Monit. Assess.* **2020**, *192*, 369. [[CrossRef](#)] [[PubMed](#)]
32. Braghieri, R.K.; Yamasoe, M.A.; Evora do Rosario, N.M.; da Rocha, H.R.; Nogueira, J.d.S.; de Araujo, A.C. Characterization of the radiative impact of aerosols on CO₂ and energy fluxes in the Amazon deforestation arch using artificial neural networks. *Atmos. Chem. Phys.* **2020**, *20*, 3439–3458. [[CrossRef](#)]
33. Bovensmann, H.; Buchwitz, M.; Burrows, J.P.; Reuter, M.; Krings, T.; Gerilowski, K.; Schneising, O.; Heymann, J.; Tretner, A.; Erzinger, J. A remote sensing technique for global monitoring of power plant CO₂ emissions from space and related applications. *Atmos. Meas. Tech.* **2010**, *3*, 781–811. [[CrossRef](#)]
34. Schwandner, F.M.; Gunson, M.R.; Miller, C.E.; Carn, S.A.; Eldering, A.; Krings, T.; Verhulst, K.R.; Schimel, D.S.; Nguyen, H.M.; Crisp, D.; et al. Spaceborne detection of localized carbon dioxide sources. *Science* **2017**, *358*, eaam5782. [[CrossRef](#)] [[PubMed](#)]
35. Shi, X.; Zheng, Y.; Lei, Y.; Xue, W.; Yan, G.; Liu, X.; Cai, B.; Tong, D.; Wang, J. Air quality benefits of achieving carbon neutrality in China. *Sci. Total. Environ.* **2021**, *795*, 148784. [[CrossRef](#)] [[PubMed](#)]
36. L'Ecuyer, T.S.; Jiang, J.H. Touring the atmosphere aboard the A-Train. *Phys. Today* **2010**, *63*, 36–41. [[CrossRef](#)]
37. Peri, F.; Volz, S. Innovative Approaches to Remote Sensing in NASA's Earth System Science Pathfinder (ESSP) Program. In *Earth Observing Systems XVIII*; Butler, J., Xiong, X., Gu, X., Eds.; SPIE: Bellingham, WA, USA, 2013; Volume 8866. [[CrossRef](#)]
38. Basilio, R.R.; Bennett, M.W.; Eldering, A.; Lawson, P.R.; Rosenberg, R.A. Orbiting Carbon Observatory-3 (OCO-3) remote sensing from the International Space Station (ISS). In *Sensors, Systems, and Nextgeneration Satellites XXIII*; Neeck, S., Martimort, P., Kimura, T., Eds.; SPIE: Bellingham, WA, USA, 2019; Volume 11151. [[CrossRef](#)]
39. Basilio, R.R.; Pollock, H.R.; Hunyadi-Lay, S.L. OCO-2 (Orbiting Carbon Observatory-2) mission operations planning and initial operations experiences. In *Sensors, Systems, and Next-Generation Satellites XVIII*; Meynart, R., Neeck, S., Shimoda, H., Eds.; SPIE: Bellingham, WA, USA, 2014; Volume 9241. [[CrossRef](#)]
40. Eldering, A.; Wennberg, P.O.; Crisp, D.; Schimel, D.S.; Gunson, M.R.; Chatterjee, A.; Liu, J.; Schwandner, F.M.; Sun, Y.; O'Dell, C.W.; et al. The Orbiting Carbon Observatory-2 early science investigations of regional carbon dioxide fluxes. *Science* **2017**, *358*, eaam5745. [[CrossRef](#)] [[PubMed](#)]
41. Crowell, S.; Baker, D.; Schuh, A.; Basu, S.; Jacobson, A.R.; Chevallier, F.; Liu, J.; Deng, F.; Feng, L.; McKain, K.; et al. The 2015–2016 carbon cycle as seen from OCO-2 and the global in situ network. *Atmos. Chem. Phys.* **2019**, *19*, 9797–9831. [[CrossRef](#)]

42. Hong, J.; Mao, F.; Min, Q.; Pan, Z.; Wang, W.; Zhang, T.; Gong, W. Improved PM_{2.5} predictions of WRF-Chem via the integration of Himawari-8 satellite data and ground observations. *Environ. Pollut.* **2020**, *263*, 114451. [[CrossRef](#)]
43. Wei, J.; Li, Z.; Sun, L.; Peng, Y.; Zhang, Z.; Li, Z.; Su, T.; Feng, L.; Cai, Z.; Wu, H. Evaluation and uncertainty estimate of next-generation geostationary meteorological Himawari-8/AHI aerosol products. *Sci. Total Environ.* **2019**, *692*, 879–891. [[CrossRef](#)]
44. Veefkind, J.P.; Aben, I.; McMullan, K.; Forster, H.; de Vries, J.; Otter, G.; Claas, J.; Eskes, H.J.; de Haan, J.F.; Kleipool, Q.; et al. TROPOMI on the ESA Sentinel-5 Precursor: A GMES mission for global observations of the atmospheric composition for climate, air quality and ozone layer applications. *Remote Sens. Environ.* **2012**, *120*, 70–83. [[CrossRef](#)]
45. Lakkala, K.; Kujanpaa, J.; Brogniez, C.; Henriot, N.; Arola, A.; Aun, M.; Auriol, F.; Bais, A.F.; Bernhard, G.; De Bock, V.; et al. Validation of the TROPospheric Monitoring Instrument (TROPOMI) surface UV radiation product. *Atmos. Meas. Tech.* **2020**, *13*, 6999–7024. [[CrossRef](#)]
46. van der Velde, I.R.; van der Werf, G.R.; Houweling, S.; Eskes, H.J.; Veefkind, J.P.; Borsdorff, T.; Aben, I. Biomass burning combustion efficiency observed from space using measurements of CO and NO₂ by the TROPospheric Monitoring Instrument (TROPOMI). *Atmos. Chem. Phys.* **2021**, *21*, 597–616. [[CrossRef](#)]
47. Douros, J.; Eskes, H.; van Geffen, J.; Boersma, K.F.; Compernelle, S.; Pinardi, G.; Blechschmidt, A.M.; Peuch, V.H.; Colette, A.; Veefkind, P. Comparing Sentinel-5P TROPOMI NO₂ column observations with the CAMS regional air quality ensemble. *Geosci. Model Dev.* **2023**, *16*, 509–534. [[CrossRef](#)]
48. Bosilovich, M.G.; Robertson, F.R.; Takacs, L.; Molod, A.; Mocko, D. Atmospheric Water Balance and Variability in the MERRA-2 Reanalysis. *J. Clim.* **2017**, *30*, 1177–1196. [[CrossRef](#)]
49. Gelaro, R.; McCarty, W.; Suarez, M.J.; Todling, R.; Molod, A.; Takacs, L.; Randles, C.A.; Darmenov, A.; Bosilovich, M.G.; Reichle, R.; et al. The Modern-Era Retrospective Analysis for Research and Applications, Version 2 (MERRA-2). *J. Clim.* **2017**, *30*, 5419–5454. [[CrossRef](#)] [[PubMed](#)]
50. Buchard, V.; Randles, C.A.; da Silva, A.M.; Darmenov, A.; Colarco, P.R.; Govindaraju, R.; Ferrare, R.; Hair, J.; Beyersdorf, A.J.; Ziemba, L.D.; et al. The MERRA-2 Aerosol Reanalysis, 1980 Onward. Part II: Evaluation and Case Studies. *J. Clim.* **2017**, *30*, 6851–6872. [[CrossRef](#)]
51. Randles, C.A.; da Silva, A.M.; Buchard, V.; Colarco, P.R.; Darmenov, A.; Govindaraju, R.; Smirnov, A.; Holben, B.; Ferrare, R.; Hair, J.; et al. The MERRA-2 Aerosol Reanalysis, 1980 Onward. Part I: System Description and Data Assimilation Evaluation. *J. Clim.* **2017**, *30*, 6823–6850. [[CrossRef](#)]
52. Guo, W.; Shi, Y.; Liu, Y.; Su, M. CO₂ emissions retrieval from coal-fired power plants based on OCO-2/3 satellite observations and a Gaussian plume model. *J. Clean. Prod.* **2023**, *397*, 136525. [[CrossRef](#)]
53. Theys, N.; De Smedt, I.; Yu, H.; Danckaert, T.; van Gent, J.; Hoermann, C.; Wagner, T.; Hedelt, P.; Bauer, H.; Romahn, F.; et al. Sulfur dioxide retrievals from TROPOMI onboard Sentinel-5 Precursor: Algorithm theoretical basis. *Atmos. Meas. Tech.* **2017**, *10*, 119–153. [[CrossRef](#)]
54. Cao, S.; Zhang, S.; Gao, C.; Yan, Y.; Bao, J.; Su, L.; Liu, M.; Peng, N.; Liu, M. A long-term analysis of atmospheric black carbon MERRA-2 concentration over China during 1980–2019. *Atmos. Environ.* **2021**, *264*, 118662. [[CrossRef](#)]
55. Shikwambana, L. Long-term observation of global black carbon, organic carbon and smoke using CALIPSO and MERRA-2 data. *Remote Sens. Letts.* **2019**, *10*, 373–380. [[CrossRef](#)]
56. Mao, M.; Zhou, Y.; Zhang, X. Evaluation of MERRA-2 Black Carbon Characteristics and Potential Sources over China. *Atmosphere* **2023**, *14*, 1378. [[CrossRef](#)]
57. Li, L.; Che, H.; Su, X.; Zhang, X.; Gui, K.; Zheng, Y.; Zhao, H.; Zhao, H.; Liang, Y.; Lei, Y.; et al. Quantitative Evaluation of Dust and Black Carbon Column Concentration in the MERRA-2 Reanalysis Dataset Using Satellite-Based Component Retrievals. *Remote Sens.* **2023**, *15*, 388. [[CrossRef](#)]

Disclaimer/Publisher’s Note: The statements, opinions and data contained in all publications are solely those of the individual author(s) and contributor(s) and not of MDPI and/or the editor(s). MDPI and/or the editor(s) disclaim responsibility for any injury to people or property resulting from any ideas, methods, instructions or products referred to in the content.